Control of cardiac alternans by mechanical and electrical feedback

Felicia Yapari,[1] Dipen Deshpande,[1] Youssef Belhamadia,[2] and Stevan Dubljevic[1,*]
[1]*Deparment of Chemical and Materials Engineering, University of Alberta, Edmonton, Alberta, T6G 2V4 Canada*
[2]*Campus Saint-Jean and Department of Mathematics, University of Alberta, Edmonton, Alberta, T6C 4G9 Canada*
(Received 14 August 2013; revised manuscript received 6 May 2014; published 25 July 2014)

A persistent alternation in the cardiac action potential duration has been linked to the onset of ventricular arrhythmia, which may lead to sudden cardiac death. A coupling between these cardiac alternans and the intracellular calcium dynamics has also been identified in previous studies. In this paper, the system of PDEs describing the small amplitude of alternans and the alternation of peak intracellular Ca^{2+} are stabilized by optimal boundary and spatially distributed actuation. A simulation study demonstrating the successful annihilation of both alternans on a one-dimensional cable of cardiac cells by utilizing the full-state feedback controller is presented. Complimentary to these studies, a three variable Nash-Panfilov model is used to investigate alternans annihilation via mechanical (or stretch) perturbations. The coupled model includes the active stress which defines the mechanical properties of the tissue and is utilized in the feedback algorithm as an independent input from the pacing based controller realization in alternans annihilation. Simulation studies of both control methods demonstrate that the proposed methods can successfully annihilate alternans in cables that are significantly longer than 1 cm, thus overcoming the limitations of earlier control efforts.

DOI: 10.1103/PhysRevE.90.012706 PACS number(s): 87.19.Hh, 05.45.−a, 87.19.R−

I. INTRODUCTION

Annually, 300 000 to 500 000 deaths in the United States can be attributed to sudden cardiac death (SCD) resulting from ventricular arrhythmias [1]. Specifically, ventricular fibrillation (VF) and ventricular tachycardia (VT) are the two types of arrhythmias associated with the abnormal electrical activities in the cardiac tissue. Both VF and VT have been identified as the primary reasons behind the majority of fatal cardiac arrest [1,2]. Alternans, shown in Fig. 1, are defined as the beat-to-beat alternation in the action potential duration (APD). Multiple studies have shown that alternans act as a precursor to these life-threatening arrhythmias, since it can transition into VF under rapid pacing rates [3–6]. On an electrocardiogram (ECG), these alternans appear as alternations in the T-wave segments. In both animals [3] and humans [7], clinical studies have shown that the risks of VF and SCD are increased in the presence of T-wave alternans, even at small levels. Therefore, the annihilation of these alternans may potentially be an effective antiarrhythmic strategy.

Alternations in the APD can be induced in the cardiac tissue by applying a rapid pacing protocol. Associated with each action potential is a resting period known as the diastolic interval (DI). Reducing the pacing period shortens the DI, and as a result the tissue does not have enough time to fully recover before the next stimulus is applied, thus yielding a shorter APD. This leads to a period-doubling bifurcation in which the following pattern emerges: short DI → short APD → long DI → long APD.

During an action potential propagation, the transmembrane potential and the intracellular Ca^{2+} transient are bidirectionally coupled [8–10]. In the case of positive $V \rightarrow Ca^{2+}$ coupling, a longer APD corresponds to a higher peak Ca^{2+} transient, and vice versa. Similarly, for positive $Ca^{2+} \rightarrow V$ coupling, a larger Ca^{2+} release will prolong the APD, and vice versa. In this work, we only consider the case when both couplings are positive, as shown in Fig. 1, which leads to concordant (spatially synchronized) alternans [9].

Most of the existing alternans annihilation methods are solely based on modulating the pacing interval at the tissue boundary. The pacing interval is modulated based on measurements of consecutive APDs at the pacing site. This electrical boundary control strategy has been shown to be effective in small tissues [3,11–13]. However, it has been shown analytically and experimentally that this control strategy has a finite degree of controllability, such that alternans stabilization in cardiac tissues >1 cm cannot be achieved [3,11–17]. One reason for this limitation is the fact that the feedback law is based on only one measurement site and therefore does not account for the spatially distributed nature of the tissue's electrical dynamics. Furthermore, since this control strategy is nonmodel based, there is an inherent limitation on the controller gain in order to prevent conduction block. As demonstrated by [18], for alternans suppression in a ring geometry, a model-based LQR (linear quadratic regulator) control scheme significantly outperforms the non-model-based control scheme. The same conclusion was reached in [19] for the open fiber (the Purkinje fiber). However, as demonstrated in [19], the optimal model-based control algorithm is only successful up to $L \approx 2$ cm. Recently, it has been shown that oscillations in the pacing cycle length can induce alternans in the heart [20]. A stochastic pacing protocol that annihilates alternans by reducing the slope of the APD resitution curve was then developed by [21]. However, this study was limited to small cardiac tissues (1 cm × 1 cm). To overcome the limitation in controllability pointed out in [16,17,19], we consider in this paper the inclusion of a second actuator which is completely independent of the boundary electrical pacing, and is based on the coupling between voltage, calcium dynamics, and the heart muscle's mechanical activity.

Previously, Dubljevic and Christofides [22] developed an optimal control strategy in which a spatially distributed,

*Corresponding author: stevan.dubljevic@ualberta.ca

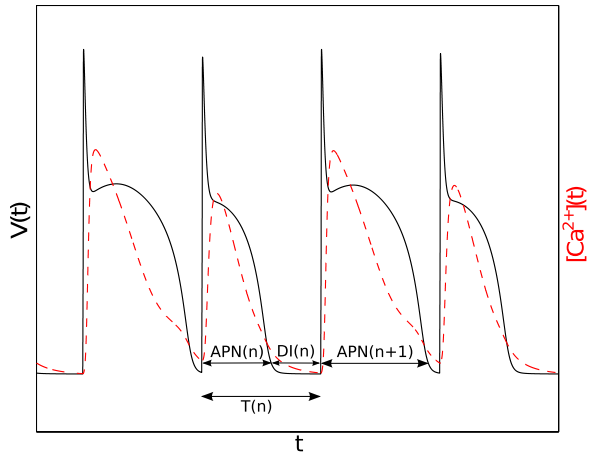

FIG. 1. (Color online) Time evolution of transmembrane potential (black solid line) and intracellular calcium concentration (red dashed line) in the presence of alternans.

calcium-based actuation was combined with boundary actuation. However, in [22], the authors did not account for the spatial evolution of the Ca^{2+} transient along the cable of cardiac cells. In this work, a similar control strategy is developed for a system of two coupled PDEs describing the spatiotemporal dynamics of the amplitudes of alternans [23] and that of the peak intracellular Ca^{2+} concentration [9]. With this coupled system of PDEs, the cardiac system's calcium dynamics is relevantly represented. These PDEs belong to a class of parabolic PDEs that describe diffusion-convection-reaction processes. By transforming the system of PDEs into an abstract evolutionary form and partitioning its spectrum into slow (finite-dimensional) and fast (infinite-dimensional) subsystems, the finite-dimensional optimal state feedback controller can be obtained, as presented in [24,25]. In this method, the boundary actuator, which represents a pacing algorithm, is applied at one end of the cable, while the calcium-based actuator is applied over a specific region of the cable. This calcium-based actuator modulates the intracellular Ca^{2+} concentration and can be realized using a drug that affects the calcium channels in the cardiac cells (tissue), delivered using either a patch or an implantable device.

The intracellular Ca^{2+} dynamics plays a critical role in the mechanical contraction and relaxation of the cardiac muscle. For instance, the binding of Ca^{2+} to Troponin C leads to the generation of active stress in the sarcomere [26]. Therefore, this coupling between the transmembrane potential and the Ca^{2+} dynamics leads to the electromechanical coupling in cardiac tissues, in which mechanically induced stretching of the tissue affects its electrical activity, and vice versa [27–29]. Specifically, [30] has demonstrated that an axial stretch in the direction of the fibers will prolong the APD.

Based on this knowledge, we develop a simple error based feedback control strategy which employs direct mechanical perturbations on the tissue, based on the three variable Nash-Panfilov (NP) model [31]. In this model, the action potential propagation is reconstructed using three variables, namely voltage, recovery, and active stress. This model is then coupled to a model of the tissue's mechanical properties, which is developed based on the finite elastic deformation theory. The resulting model is a fully coupled electromechanical model for the contracting excitable tissue, in which the effects of mechanoelectric feedback are incorporated systematically. The control action for this method is applied to the model's active stress variable, using an error based control algorithm in which the error signal is the difference between two consecutive APD measurements. The mechanoelectric feedback is achieved through a stretch-activated current, which is dependent on the active stress variable. Thus, modulating the active stress variable alters the tissue's electric wave profile, and consequently the APD. To the authors' best knowledge, this method of alternans annihilation has not been explored in previous studies. Through numerical simulations, we demonstrate that both control algorithms can successfully annihilate alternans in the whole cable of cardiac cells with length $\gg 1$ cm.

Finally, the main contribution of the research efforts demonstrated in this work is to extend the understanding and to provide theoretical analysis for the idea of a combined pacing and mechanoelectric (Ca^{2+})-based alternans annihilation in relevantly sized cardiac tissue. The dynamical analysis of spatiotemporal voltage and calcium coupling arising from relevant ionic models (LR1, Fox, etc.) and model based control synthesis provide a foundation to seek alternans annihilation realizations in the cardiac tissue of size greater than 1 cm. In particular, a fully coupled electromechanical model is utilized to demonstrate the mechanic based annihilation of alternans.

This paper is organized as follows. Section II introduces the amplitude of alternans PDEs and the system's state space representation. Section III is devoted to the optimal control of cardiac alternans and its realization through numerical simulations, where parameters emerging from two ionic models are considered. The limitations of this approach are also discussed in this section. Finally, Sec. IV is dedicated to the control and numerical realization of the electromechanical model.

II. PRELIMINARIES

A. Amplitude equations

A cable of cardiac cells can be modeled as an excitable medium, and the propagation of action potentials along the cable is described by the following cable equation:

$$\frac{\partial V(\zeta,t)}{\partial t} = D\frac{\partial^2 V(\zeta,t)}{\partial \zeta^2} - \frac{I_{\text{ion}}(\zeta,t)}{C_m} \tag{1}$$

with boundary conditions

$$\frac{\partial V(0,t)}{\partial \zeta} = V_p(t), \quad \frac{\partial V(L,t)}{\partial \zeta} = 0. \tag{2}$$

The first term on the right hand side of (1) describes the propagation of action potential from one cell to another due to the diffusive coupling between the cells. $I_{\text{ion}}(\zeta,t)$ represents the sum of the ionic currents that passes through the cell membrane during an action potential, and its formulation varies from one ionic model to another. $V_p(t) = I_{\text{stim}}/C_m$ is the electrical stimulus applied at one end of the cable. Finally, $D = 0.001$ cm^2/ms and $C_m = 1$ μF/cm^2 are the diffusivity

constant and the cell membrane capacitance, respectively. In this work, two ionic models are considered, namely the Luo-Rudy (LR1) model given in [32] and the Fox model presented in [33]. The main difference between these two ionic models lies in the treatment of the intracellular Ca^{2+} dynamics. The Fox ionic model explicitly accounts for the bidirectional coupling between the transmembrane potential and the intracellular Ca^{2+} concentration, while the LR1 model does not.

The amplitude of alternans, $a(\zeta,n)$, is defined as the difference between two consecutive APDs. That is,

$$a(\zeta,n) = (\mathrm{APD}_{\zeta,n} - \mathrm{APD}_{\zeta,n-1})(-1)^n. \tag{3}$$

Using the fact that close to the critical pacing rate, $a(\zeta,n)$ varies slowly from beat to beat, Echebarria and Karma [23] derived the PDE that describes the spatiotemporal dynamics of the small amplitude of alternans. Similarly, based on [9], a PDE describing the spatiotemporal dynamics of the peak intracellular Ca^{2+}, denoted as $a_{Ca}(\zeta,t)$, can be written. For a 1D cable, the system of PDEs is given by

$$\frac{\partial a(\zeta,t)}{\partial t} = D_{a_1}\frac{\partial^2 a(\zeta,t)}{\partial \zeta^2} - \omega_1\frac{\partial a(\zeta,t)}{\partial \zeta} + \sigma a(\zeta,t) - g a(\zeta,t)^3 + \eta a_{Ca}(\zeta,t), \tag{4}$$

$$\frac{\partial a_{Ca}(\zeta,t)}{\partial t} = D_{a_2}\frac{\partial^2 a_{Ca}(\zeta,t)}{\partial \zeta^2} - \omega_2\frac{\partial a_{Ca}(\zeta,t)}{\partial \zeta} + \gamma a(\zeta,t) + \sum_{i=1}^{m} b_{Ca,i}(\zeta)u_{Ca,i}(t), \tag{5}$$

with boundary conditions

$$\frac{\partial a(0,t)}{\partial \zeta} = a(0,t) + v(t), \quad \frac{\partial a(L,t)}{\partial \zeta} = 0, \tag{6}$$

$$\frac{\partial a_{Ca}(0,t)}{\partial \zeta} = a_{Ca}(0,t) \quad \frac{\partial a_{Ca}(L,t)}{\partial \zeta} = 0. \tag{7}$$

All the PDE parameters are normalized with respect to τ, the pacing period. In both (4) and (5), the parameters D_{a_i} and ω_i describe the propagation of the amplitudes by diffusion and convection, respectively. Although there is no diffusion of Ca^{2+} between the adjacent cells, we expect that the alternations in $a_{Ca}(\zeta,t)$ will propagate along the cable in a similar fashion to that of $a(\zeta,t)$ due to the bidirectional coupling between them. Therefore, it is assumed that $D_{a_1} = D_{a_2} = D_a$ and $\omega_1 = \omega_2 = \omega$. The term $\sigma a(\zeta,t)$ represents the growth of the amplitude of alternans along the cable, while the term $g a(\zeta,t)^3$ ensures that the evolution of $a(\zeta,t)$ is bounded. In this work, we assume that alternans arise from the instabilities in the voltage dynamics and not the Ca^{2+} dynamics. Therefore, these terms are omitted in (5). Finally η and γ are the coupling parameters that relate the two PDEs.

The boundary actuation, which represents a pacing protocol applied at $\zeta = 0$, is denoted by $v(t)$, while the spatially distributed actuation is denoted by $u_{Ca}(t)$. This calcium-based actuation acts directly on the $a_{Ca}(\zeta,t)$ system in order to suppress the alternations in the intracellular Ca^{2+} concentration, but also helps in stabilizing the $a(\zeta,t)$ system through the coupling between the two PDEs. The placement

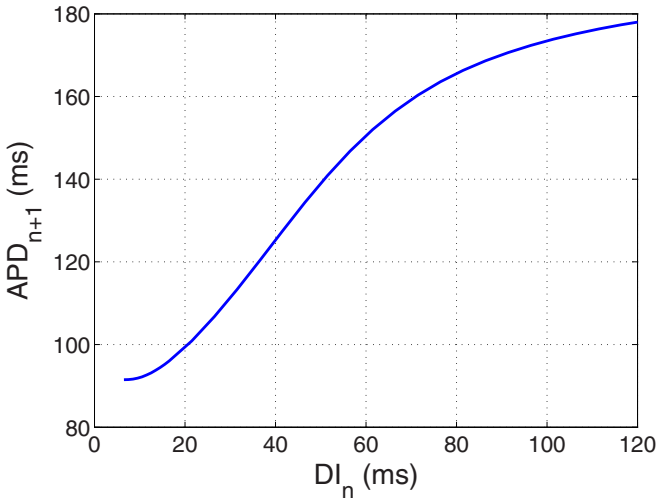

FIG. 2. (Color online) Restitution curve for the Fox ionic model obtained using an S1 period of 350 ms and S2 periods ranging from 340 to 200 ms.

of the ith calcium-based actuator on the cable is described by the function $b_{Ca,i}(\zeta)$, and the summation term in Eq. (5) represents the overall effect of the calcium-based actuator(s) on the system.

The parameters D_a, ω, σ, and g are obtained from the restitution curve, which describes the relationship between the $(n+1)$th APD and the previous DI, i.e., $\mathrm{APD}^{n+1} = f(\mathrm{DI}^n)$. The restitution curve for the Fox ionic model is shown in Fig. 2. This figure was obtained by applying the S1S2 pacing protocol to a single cardiac cell. In this protocol, the cell is initially paced at a sufficiently large pacing cycle length (PCL_{S1}) for 50 beats, followed by a shorter cycle length (PCL_{S2}). This is repeated for decreasing values of PCL_{S2}, until conduction block is induced. The electrical stimulus is applied as square wave pulses with a magnitude of 80 μA/μF and a duration of 1 ms [33]. The APD was measured as APD90, which is the APD at 90% repolarization.

Based on [23], the PDE parameters are defined as $D_a \approx \sqrt{D \times \mathrm{APD}_c}$, $\omega \approx 2D/c$, $\sigma \approx \ln(f')$ and $g \approx (f'')^2/4 - f'''/6$, with all derivatives computed at the bifurcation point, defined as the pacing period at which persistent alternans start to emerge. APD_c is the APD at the bifurcation point, and c is the wave propagation speed computed at the bifurcation point. Refer to [23] for the detailed derivation and physical interpretation of these parameters. To identify γ, the S1S2 pacing protocol described previously is again applied to the single cell, and the peak Ca^{2+} concentration at S2 is plotted against the DI at S1. γ is then obtained by computing the slope of this curve at the bifurcation point. The identification of η is performed by pacing the single cell at a period close to the the bifurcation point for approximately 50 beats, and then introducing an external Ca^2+ signature (obtained from a separate simulation with a different pacing period) for the following beat. η is then approximated by the ratio $\frac{\Delta a}{\Delta a_{Ca}}$. Note that since the LR1 model does not account for the coupling between $a_{Ca}(\zeta,t)$ and the transmembrane potential, η for this model is set to zero.

B. Amplitude of voltage and calcium alternans representation

For the following procedure, the PDEs given by (4)–(7) are first linearized around their spatially uniform unstable steady states $a(\zeta,t) = 0$ and $a_{Ca}(\zeta,t) = 0$. Equations (4) and (6) can then be formulated as the following abstract boundary control problem:

$$\begin{aligned} \frac{da}{dt} &= \mathcal{F}a(t) + \eta a_{Ca}(t), \quad t \geqslant 0, \\ a(0) &= a_0, \quad \mathcal{B}a(t) = v(t), \end{aligned} \tag{8}$$

where $a(\cdot,t) = \{a(\zeta,t), 0 \leqslant \zeta \leqslant L\}$ and $a_{Ca}(\cdot,t) = \{a_{Ca}(\zeta,t), 0 \leqslant \zeta \leqslant L\}$ are state variables in the Hilbert space $\mathcal{L}_2([0,L];t)$ [24], t is the time variable, and $v(t) \in \mathbb{R}$ is the boundary actuation. $\mathcal{F}$ is the spatial derivative operator defined as

$$\mathcal{F}\phi(\zeta) = \left[D_a \frac{d^2}{d\zeta^2} - w\frac{d}{d\zeta} + \sigma \right]\phi(\zeta) \tag{9}$$

with the domain $\mathcal{D}(\mathcal{F}) = \{\phi(\zeta) \in L_2(0,L) : \phi(\zeta), \phi'(\zeta)$ are absolutely continuous, $\mathcal{F}\phi(\zeta) \in L_2(0,L)$, and $\phi'(L) = 0\}$. Here $L_2(0,L)$ denotes the Hilbert space of measurable, square-integrable, real-valued functions with weighted inner product and norm defined as $\langle f,g\rangle_{\mu,L_2} = \int_0^L e^{-\mu\zeta} f(\zeta)g(\zeta)d\zeta$, and $\|f\|_2 = \sqrt{\langle f,f\rangle_{\mu,L_2}}$, respectively. The boundary operator $\mathcal{B} : L_2(0,L) \mapsto \mathbb{R}$ can be defined as follows:

$$\mathcal{B}\phi(\zeta) = \frac{\delta\phi(0)}{\delta\zeta} - \phi(0), \quad \text{with} \quad \mathcal{D}(\mathcal{F}) \subset \mathcal{D}(\mathcal{B}). \tag{10}$$

Equation (8) is not well posed, due to the fact that the controlled input appears in the boundary condition. Therefore, we define a new operator $\mathcal{A}_1$ such that

$$\mathcal{A}_1\phi(\zeta) = \mathcal{F}\phi(\zeta), \quad \text{and} \quad \mathcal{D}(\mathcal{A}_1) = \mathcal{D}(\mathcal{F}) \cup \ker(\mathcal{B}). \tag{11}$$

This is based on the assumption that $v(t) \in \mathbf{C^2}([0,t];V)$ is sufficiently smooth, and one can find a function $B(\zeta)$ such that $\forall v(t)$, $B(\zeta)v(t) \in \mathcal{D}(\mathcal{F})$, and

$$\mathcal{B}B(\zeta)v(t) = v(t), \quad v(t) \in V. \tag{12}$$

Furthermore, without loss of generality, we can choose $B(\zeta)$ such that $\mathcal{F}B(\zeta) = 0$. Knowing $B(\zeta)$, we define the following state transformation:

$$a(t) = p(t) + B(\zeta)v(t). \tag{13}$$

Substituting (13) into (8), we obtain the following well posed abstract differential equation:

$$\begin{aligned} \frac{dp}{dt} &= \mathcal{A}_1 p(t) + \mathcal{F}Bv(t) + \eta a_{Ca}(t) - B\dot{v}(t), \quad t \geqslant 0, \\ p(0) &= p_0. \end{aligned} \tag{14}$$

Interestingly, in (14), the boundary actuation is manifested as a time derivative when it is transferred into the domain of the PDE setting. This can be seen as a constraint on the pacing protocol, since $\dot{v}(t)$ needs to be a sufficiently smooth function. Additionally, it is important to note that the transformation given by (13) must be exact to ensure that any noise at the boundary will not be amplified throughout the system.

A similar abstract evolutionary form can be formulated for the $a_{Ca}(\zeta,t)$ PDE:

$$\begin{aligned} \frac{da_{Ca}}{dt} &= \gamma a(t) + \mathcal{A}_2 a_{Ca}(t) + \mathcal{B}_{Ca}u_{Ca}(t), \quad t \geqslant 0, \\ a_{Ca}(0) &= a_{Ca_0}, \end{aligned} \tag{15}$$

where the spatial derivative operator $\mathcal{A}_2$ is given by

$$\mathcal{A}_2\psi(\zeta) = \left[D_a \frac{d^2}{d\zeta^2} - w\frac{d}{d\zeta} \right]\psi(\zeta) \tag{16}$$

with the domain $\mathcal{D}(\mathcal{A}_2) = \{\psi(\zeta) \in L_2(0,L) : \psi(\zeta), \psi'(\zeta)$ are abs. cont., $\mathcal{A}_2\psi(\zeta) \in L_2(0,L), \psi'(0) - \psi(0) = 0$, and $\psi'(L) = 0\}$. For the spatially distributed actuators, we define

$$\mathcal{B}_{Ca}u_{Ca}(t) = \sum_{i=1}^{n} b_{Ca,i}(\zeta)u_{Cai}(t), \tag{17}$$

where $b_{Ca,i}(\zeta) = \frac{1}{2\epsilon}$ for $\zeta \in [\zeta_i - \epsilon, \zeta_i + \epsilon]$, $\epsilon > 0$ is a function describing the locations of the actuators.

Combining (14) and (15), and defining $v(t)$ as a new state variable, the PDE system given by (4)–(7) is reformulated on the extended state space $L_2^e := L_2 \otimes V$, yielding

$$\begin{aligned} \dot{a}^e(t) &= \begin{bmatrix} 0 & 0 & 0 \\ \mathcal{F}B & \mathcal{A}_1 & \eta \\ \gamma B & \gamma & \mathcal{A}_2 \end{bmatrix} a^e(t) + \begin{bmatrix} 1 & 0 \\ -B & 0 \\ 0 & \mathcal{B}_{Ca} \end{bmatrix} \begin{bmatrix} \tilde{v}(t) \\ u_{Ca}(t) \end{bmatrix} \\ &= \mathcal{A}^e a^e(t) + \mathcal{B}^e\tilde{u}(t), \\ a^e(0) &= [v(0) \quad p(0) \quad a_{Ca}(0)]' = a_0^e. \end{aligned} \tag{18}$$

Here, $a^e = [v(t) \quad p(t) \quad a_{Ca}(t)]'$ and $\tilde{v}(t) = \dot{v}(t)$. Physiologically, $\tilde{v}(t)$ can be interpreted as the rate of change of pacing period applied at the boundary.

By solving the eigenvalue problem $\mathcal{A}\phi(\zeta) = \lambda\phi(\zeta)$, the eigenvalues and corresponding eigenfunctions of $\mathcal{A}_1$ and $\mathcal{A}_2$ can be found analytically through the separation of variables [24]. Furthermore, eigenfunctions of the adjoint operators $\mathcal{A}_1^*$ and $\mathcal{A}_2^*$ that satisfy the orthogonality condition $\langle\phi_i(\zeta), \phi_j^*(\zeta)\rangle = \delta_{ij}$ can also be computed. The eigenvalues for $\mathcal{A}_1$ and $\mathcal{A}_2$ are respectively given by

$$\lambda_i = \sigma - D_a\left[\alpha_i + \frac{\omega^2}{4D_a^2}\right], \quad 0 < \alpha_i < \alpha_{i+1}, \quad i \geqslant 1, \tag{19}$$

$$\bar{\lambda}_i = -D_a\left[\alpha_i + \frac{\omega^2}{4D_a^2}\right], \quad 0 < \alpha_i < \alpha_{i+1}, \quad i \geqslant 1, \tag{20}$$

where α_i are the solutions to the following transcendental equation:

$$\tan(\sqrt{\alpha_i}L) = \frac{\sqrt{\alpha_i}}{\alpha_i - \frac{\omega}{2D_a}\left(1 - \frac{\omega}{2D_a}\right)}. \tag{21}$$

The corresponding eigenfunctions for $\mathcal{A}_1$ and $\mathcal{A}_2$ are denoted by $\phi_i(\zeta)$ and $\psi_i(\zeta)$, respectively. These are given in Appendix A, along with the adjoint eigenfunctions $\phi_i^*(\zeta)$ and $\psi_i^*(\zeta)$.

In general, the eigenvalues and eigenfunctions of $\mathcal{A}^e$ cannot be determined analytically. However, in the special case where $\eta = 0$ (i.e., the LR1 case), $\mathcal{A}^e$ has a lower triangular structure. In this case, the eigenvalue problem for this extended operator

can be solved analytically. First, note that $\mathcal{A}^e$ can be written as

$$\mathcal{A}^e = \begin{bmatrix} 0 & 0 \\ A_3 & \mathcal{A} \end{bmatrix}, \quad \text{with} \quad \mathcal{A} = \begin{bmatrix} \mathcal{A}_1 & 0 \\ \gamma & \mathcal{A}_2 \end{bmatrix}$$

$$\text{and} \quad A_3 = \begin{bmatrix} \mathcal{F}B \\ B \end{bmatrix}.$$

Since $\mathcal{A}$ is a lower triangular matrix, its eigenspectrum is given by $\Omega(\mathcal{A}) = \Omega(\mathcal{A}_1) \cup \Omega(\mathcal{A}_2)$. That is,

$$\Omega(\mathcal{A}) = \Lambda_j = \begin{cases} \lambda_i & \text{when } j \text{ is odd,} \\ \bar{\lambda}_i & \text{when } j \text{ is even.} \end{cases} \tag{22}$$

Denoting the eigenfunctions of $\mathcal{A}$ as $\Phi_j(\zeta) = [\xi_{1,j} \;\; \xi_{2,j}]'$, we have

$$\begin{bmatrix} \mathcal{A}_1 & 0 \\ \gamma & \mathcal{A}_2 \end{bmatrix} \begin{bmatrix} \xi_{1,j} \\ \xi_{2,j} \end{bmatrix} = \Lambda_j \begin{bmatrix} \xi_{1,j} \\ \xi_{2,j} \end{bmatrix}. \tag{23}$$

Equation (23) leads to a system of two algebraic equations for each value of Λ_j. Solving these equations, and utilizing the definition of resolvent sets [24], we obtain the following expression:

$$\Phi_j(\zeta) = \begin{cases} \left[\phi_i(\zeta) \quad \frac{\gamma}{\sigma}\psi_i(\zeta)\right]', & \text{when } j \text{ is odd,} \\ [0 \quad \psi_i(\zeta)]', & \text{when } j \text{ is even.} \end{cases} \tag{24}$$

The eigenfunctions of the adjoint operator $\mathcal{A}^*$ can be found using the same procedure. These are given by

$$\Psi_j(\zeta) = \begin{cases} [\phi_i^*(\zeta) \quad 0]', & \text{when } j \text{ is odd,} \\ \left[-\frac{\gamma}{\sigma}\phi_i^*(\zeta) \quad \psi_i^*(\zeta)\right]', & \text{when } j \text{ is even.} \end{cases} \tag{25}$$

The same procedure is again repeated for the extended spatial operator $\mathcal{A}^e$, whose eigenspectrum is given by $\Omega(\mathcal{A}^e) = \{0\} \cup \Omega(\mathcal{A}) = \{0\} \cup \{\lambda_i\} \cup \{\bar{\lambda}_i\}$. If there are m boundary input variables, the zero eigenvalue will be repeated m times. Here, $m = 1$. The eigenfunction and adjoint eigenfunction corresponding to the zero eigenvalue are given by

$$\hat{\Phi}_0(\zeta) = \begin{bmatrix} 1 \\ \sum_{j=1}^{\infty} \frac{1}{\Lambda_j}\langle A_3, \Psi_j \rangle \Phi_j \end{bmatrix} \quad \text{and} \quad \hat{\Psi}_0(\zeta) = \begin{bmatrix} 1 \\ 0 \end{bmatrix} \tag{26}$$

while those corresponding to the remaining eigenvalues are given by

$$\hat{\Phi}_j(\zeta) = \begin{bmatrix} 0 \\ \Phi_j \end{bmatrix} \quad \text{and} \quad \hat{\Psi}_j(\zeta) = \begin{bmatrix} \frac{1}{\Lambda_j} A_3^* \Psi_j \\ \Psi_j \end{bmatrix}. \tag{27}$$

Parabolic systems such as (4)–(7) can be realized through modal decomposition. In the case where the PDE parameters are obtained from the LR1 model, the decomposition can be performed directly on the extended state a^e, since the eigenfunctions of $\mathcal{A}^e$ can be found analytically, as given by (26) and (27). By substituting $a^e = \sum_{j=1}^{\infty} c_j(t)\hat{\Phi}_j(\zeta)$ into (18) and projecting the resulting system onto $\hat{\Psi}_j(\zeta)$, we obtain the following infinite-dimensional state space system:

$$\dot{c}(t) = \Lambda c(t) + \langle \mathcal{B}^e, \hat{\Psi}(\zeta) \rangle \tilde{u}(t), \tag{28}$$

where Λ is a diagonal matrix whose entries are the eigenvalues of $\mathcal{A}^e$.

On the other hand, when the PDE parameters are obtained using the Fox model, analytical expressions for $\hat{\Phi}_j(\zeta)$ and $\hat{\Psi}_j(\zeta)$ are not available. Therefore, each state variable must be decomposed separately, namely $a(\zeta,t) = \sum_{i=1}^{\infty} a_i(t)\phi_i(\zeta)$ and $a_{Ca}(\zeta,t) = \sum_{i=1}^{\infty} a_{Ca_i}(t)\psi_i(\zeta)$. After applying the state transformation (13) and substituting these eigenfunction expansions into (18), for each i we obtain

$$\begin{bmatrix} 1 & 0 & 0 \\ 0 & \phi_i & 0 \\ 0 & 0 & \psi_i \end{bmatrix} \dot{a}_i^e = \mathcal{A}_i^e \begin{bmatrix} 1 & 0 & 0 \\ 0 & \phi_i & 0 \\ 0 & 0 & \psi_i \end{bmatrix} a_i^e + \mathcal{B}^e \tilde{u}. \tag{29}$$

Projecting (29) onto

$$\begin{bmatrix} 1 & 0 & 0 \\ 0 & \phi_i^* & 0 \\ 0 & 0 & \psi_i^* \end{bmatrix},$$

we obtain

$$\begin{aligned} \dot{a}_i^e(t) &= \begin{bmatrix} 0 & 0 & 0 \\ \langle \mathcal{F}B, \phi_i^* \rangle & \lambda_i & \eta \\ \langle B, \psi_i^* \rangle & \gamma & \bar{\lambda}_i \end{bmatrix} a_i^e(t) \\ &\quad + \begin{bmatrix} 1 & 0 \\ -\langle B, \phi_i^* \rangle & 0 \\ 0 & \langle b_j, \psi_i^* \rangle \end{bmatrix} \tilde{u}(t) \\ &= A^e a_i^e(t) + B^e \tilde{u}(t). \end{aligned} \tag{30}$$

In this case, the overall system's eigenvalues must be computed numerically. Nonetheless, it is still possible to diagonalize the state matrix A^e using its eigenvectors, since all the eigenvalues are distinct. These eigenvalues are dependent on the coupling parameters η and γ. When η and γ have opposite signs, depending on their magnitudes, one can potentially obtain conjugate complex eigenvalues, which will result in oscillatory coupling among the APD and calcium alternans. However, further parametric investigation is required to determine whether or not this can be realistically achieved. In this study, both η and γ are positive, and all eigenvalues are real.

The stability of the extended system given by (18) is governed by the eigenvalues of $\mathcal{A}^e$, which are dependent on the eigenvalues of the individual PDEs, namely λ_i and $\bar{\lambda}_i$. From (20), it is apparent that $\forall i$, $\bar{\lambda}_i < 0$. This implies that in the absence of coupling, (5) is inherently stable. For the LR1 case, the overall system's eigenvalues are simply a union of λ_i and $\bar{\lambda}_i$ [see (22)]. Therefore, in this case, due to the master-slave relationship between voltage and calcium dynamics, instabilities in the extended system arise solely from the $a(\zeta,t)$ (voltage) subsystem. On the other hand, for the Fox model, each of the overall system's eigenvalues depend simultaneously on both λ_i and $\bar{\lambda}_i$. As a result, due to the bidirectional coupling between voltage and calcium dynamics, both subsystems contribute to the instabilities in the extended system.

III. OPTIMAL CARDIAC ALTERNANS ANNIHILATION

The operators of the parabolic system given by (4)–(7) are dissipative, and the structure of their eigenspectra is beneficial for the formulation of a simple gain-based optimal full-state feedback control law which stabilizes the unstable modes, while the stable modes remain invariant to this control law. The eigenspectrum of $\mathcal{A}^e$ can be divided into a finite-dimensional unstable (slow) part and an infinite-dimensional stable (fast) part, i.e., $\Omega(\mathcal{A}^e) = \Omega^+(\mathcal{A}^e) \cup \Omega^-(\mathcal{A}^e)$. The finite-dimensional

TABLE I. PDE parameter values for the LR1 and Fox ionic models.

	LR1	Fox
D_a	0.4883	0.148
ω	0.03388	0.04
σ	ln(2.2)	ln(1.314)
g	0	7.221×10^{-5}
η	0	0.6
γ	2.25×10^{-6}	8.575×10^{-3}

optimal controller will then be developed based only on the unstable subsystem.

The optimal controller gain is obtained by solving the following minimization problem over an infinite time horizon:

$$\min_{\tilde{u}} J(a^e(0);\tilde{u}) = \int_0^\infty \left[a_u^e(t)' Q a_u^e + \tilde{u}(t)' R \tilde{u}(t)\right] dt,$$
$$\text{subject to} \quad \dot{a}_u^e(t) = \mathcal{A}_u^e a_u^e(t) + \mathcal{B}_u^e \tilde{u}(t), \tag{31}$$

where $a_u^e(t)$, $\mathcal{A}_u^e$ and $\mathcal{B}_u^e$ have dimensions corresponding to that of the unstable subsystem $\Omega^+(\mathcal{A}^e)$. $Q \geqslant 0$ and $R > 0$ are the diagonal penalty matrices for the state and input variables, respectively. Solving this LQR problem, the optimal control law is obtained as

$$\tilde{u}_{\text{opt}}(t) = -K_{\text{opt}} a_u^e(t) = -\tfrac{1}{2} R^{-1} B_u^{'} P a_u^e(t), \tag{32}$$

where P is a symmetric, positive definite solution to the algebraic Riccati equation

$$0 = A_u^{'} P + P A_u + Q - P B_u R^{-1} B_u^{'} P. \tag{33}$$

A. Numerical simulation

In this section, we consider the system of PDEs given by (4)–(7), with parameters D_a, ω, σ, and g obtained from the LR1 ionic model [32] and the Fox ionic model [33]. These parameters as well as the coupling parameters η and γ are presented in Table I. The critical pacing periods for the LR1 model and the Fox model were found to be 311 and 215 ms, respectively. For the each set of parameters, the eigenspectra for the operators $\mathcal{A}_1$ and $\mathcal{A}_2$ are computed according to (19)–(21). The eigenspectrum of $\mathcal{A}^e$ can then be obtained from these individual eigenvalues. The distribution of the eigenspectrum depends on the cable length L. As can be seen from Figs. 3 and 4, the number of unstable eigenvalues increases with increasing cable length. In these simulations, a cable length of 6.25 cm is considered. Both Figs. 3 and 4 show that for all cable lengths, there is a zero eigenvalue. This is because for both models, $\Omega(\mathcal{A}^e) = \{0\} \cup \Omega(\mathcal{A})$, where the zero eigenvalue arises from the presence of boundary actuation. This is a dynamical feature that has not been recognized in previous works, and implies that the system is effectively controlled by the time derivative of the boundary input and not the input itself.

In both cases, the Galerkin formulations for $a(\zeta,t)$ and $a_{Ca}(\zeta,t)$ are approximated by 28 modes, namely $a(\zeta,t) = \sum_{i=1}^{28} a_i(t)\phi_i(\zeta)$ and $a_{Ca}(\zeta,t) = \sum_{i=1}^{28} a_{Ca_i}(t)\psi_i(\zeta)$. This leads

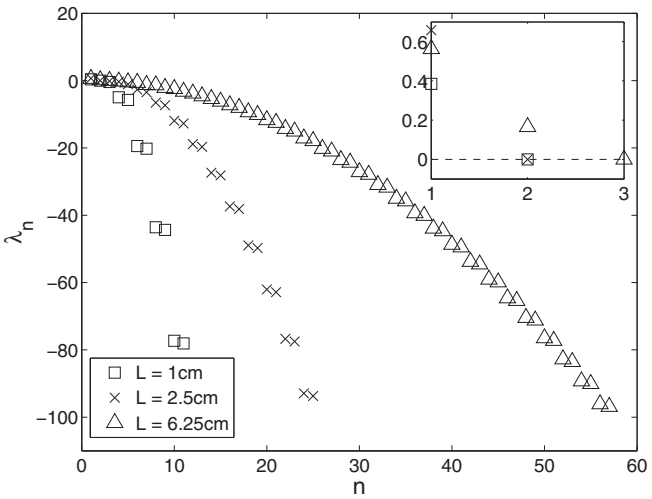

FIG. 3. Eigenspectrum of $\mathcal{A}^e$ for the LR1 model, for different cable lengths.

to a finite-dimensional approximation to (18), of the form

$$\dot{a}^e(t) = \bar{A}^e a^e(t) + \bar{B}^e \tilde{u}(t), \tag{34}$$

where $\bar{A}^e$ and $\bar{B}^e$ are (57×57) and (57×2) matrices, respectively. Increasing the number of modes in the Galerkin formulation will increase the number of fast modes, which are stable. Since the controller formulation is based only on the slow modes, increasing the total number of modes will not affect the overall result. The function $B(\zeta)$ has the general form

$$B(\zeta) = \exp^{a\zeta}[c_1 \cos(b\zeta) + c_2 \sin(b\zeta)], \tag{35}$$

where a and b are the real and imaginary parts of r, which satisfy the characteristic equation of (4):

$$D_a r^2 - \omega r + \sigma = 0. \tag{36}$$

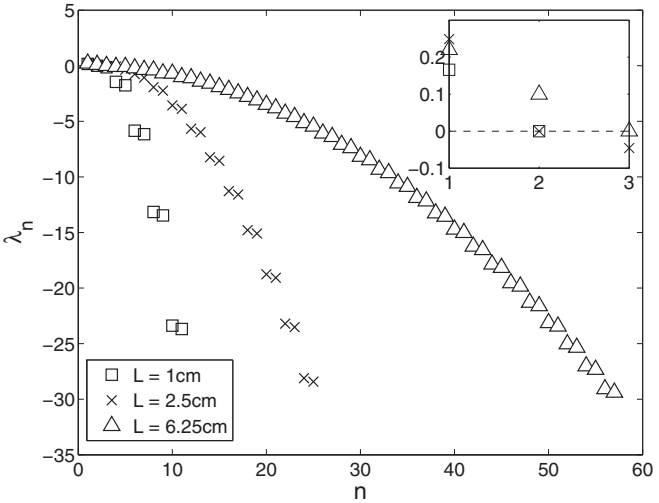

FIG. 4. Eigenspectrum of $\mathcal{A}^e$ for the Fox ionic model, for different cable lengths.

The coefficients c_1 and c_2 can be found by applying the following boundary conditions:

$$\left.\frac{dB}{d\zeta}\right|_{\zeta=0} - B(0) = 1, \quad \left.\frac{dB}{d\zeta}\right|_{\zeta=L} = 0. \tag{37}$$

The Ca^{2+} based controller, $u_{Ca}(t)$, is applied at $\zeta \in [3.5,4.5]$ cm. The location of this actuator was chosen to be far enough from the boundary, such that its effects are independent from the boundary pacer. In choosing the size of this region, we have considered the trade-off between the magnitude of actuation and the size of the actuator. This size was therefore selected such that the magnitude of actuation is not too high, while keeping the affected region relatively small.

Once the finite-dimensional approximation of the system has been obtained, the system is decomposed into the stable (fast) and unstable (slow) subsystems. The low-dimensional unstable subsystem is then used to compute the optimal control law, given by (32). Computation of the optimal control law requires solving the algebraic Riccati equation. This is done through MATLAB using the "*care* "function. Note that in this procedure, the nonlinear term in (4) is neglected. However, since this term has a stabilizing effect on the system, this exclusion has no negative effect on the stability of the closed loop system. In the simulations, this nonlinear term is added to the closed loop system as $\mathcal{G}_i(t) = g\langle a(\zeta,t)^3, \psi_i(\zeta)\rangle$. The same penalty matrices are used in both cases. Q can be partitioned as $Q = [q_v \;\; 0; \;\; 0 \;\; q_a I]$, where $q_v = 10$ is applied to $v(t)$ and $q_a = 5$ is applied to $p(t)$ and $a_{Ca}(t)$. For the input variables, an equal weight is placed on $\tilde{v}(t)$ and $u_{Ca}(t)$: $R = [5 \;\; 0; \;\; 0 \;\; 5]$. The numerical integration is performed using the explicit finite difference method with $\Delta t = 0.02$.

Case 1: LR1 ionic model

For the parameter values given in Table I and a cable length of 6.25 cm, $\mathcal{A}^e$ has three unstable eigenvalues (including the zero eigenvalue). As discussed previously, all the unstable eigenvalues correspond to those of $\mathcal{A}_1$. Therefore, for the LR1 model, the $a_{Ca}(\zeta,t)$ PDE (5) is inherently stable, and only (4) needs to be stabilized.

The finite-dimensional approximation of the system, (34), takes the form of (28), where the $\bar{A}^e$ and $\bar{B}^e$ can be computed by following the procedure outlined in (22)–(27). Since there are three unstable modes, a third-order optimal controller is obtained. Solving the LQR problem posed in (31), we obtained the following optimal controller gain:

$$K_{\text{opt}} = \begin{bmatrix} 1 & -23.3 & 4.61 \\ 0 & 0 & 0 \end{bmatrix}. \tag{38}$$

As noted earlier, since the $a_{Ca}(\zeta,t)$ system is already stable, $u_{Ca}(t)$ is deemed unnecessary in this case, and therefore the corresponding controller gains are equal to zero. Applying this controller gain to (34) [via Eq. (32)], we obtained the closed loop response for $a(\zeta,t)$, shown in Fig. 5. This figure shows that the low-dimensional controller can indeed stabilize all 28 modes of $a(\zeta,t)$. The corresponding trajectories of $v(t)$ and $\tilde{v}(t)$ are shown in Figs. 8 and 9.

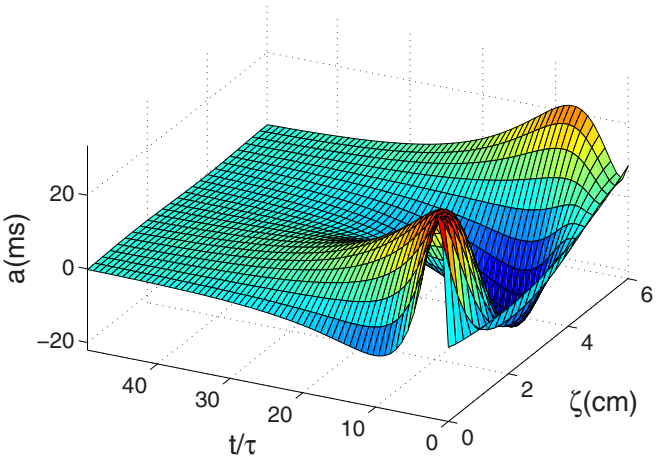

FIG. 5. (Color online) Stabilization of the amplitude of alternans PDE under optimal full-state feedback control with LR1 model parameters.

Case 2: Fox ionic model

In this case, despite the fact that all the eigenvalues of $\mathcal{A}_2$ are negative, instabilities can still arise in the $a_{Ca}(\zeta,t)$ system due to the bidirectional coupling between (4) and (5). Using the parameter values in Table I, we found that $\mathcal{A}^e$ has three unstable eigenvalues. Therefore, both $a(\zeta,t)$ and $a_{Ca}(\zeta,t)$ need to be stabilized.

As noted in the previous section, analytical expressions for the eigenvalues and eigenfunctions of $\mathcal{A}^e$ are not available when η is nonzero. Therefore, $\bar{A}^e$ and $\bar{B}^e$ must be computed according to (30). A state transformation was then performed to diagonalize $\bar{A}^e$ before the unstable subsystem was extracted. The remaining procedure for obtaining the optimal control law is identical to that employed in the LR1 case. Here, the optimal controller gain was found to be

$$K_{\text{opt}} = \begin{bmatrix} 0.469 & -11.2 & 2.46 \\ -0.957 & -10.1 & 1.54 \end{bmatrix}. \tag{39}$$

In contrast to the previous case, the second row of K_{opt} is now nonzero since the $a_{Ca}(\zeta,t)$ system is also unstable. Figures 6 and 7 show the stabilization of $a(\zeta,t)$ and $a_{Ca}(\zeta,t)$,

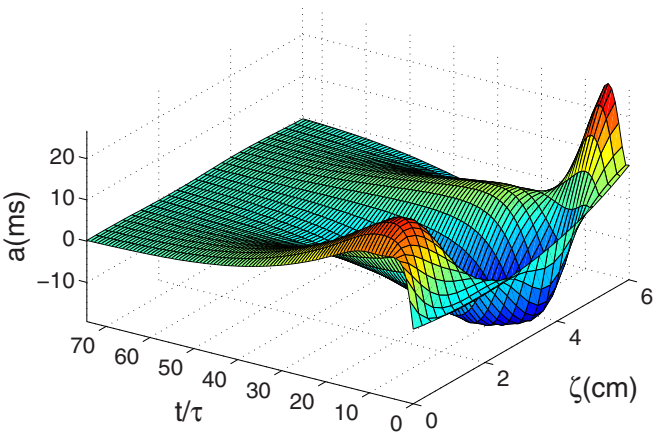

FIG. 6. (Color online) Stabilization of the amplitude of alternans PDE under optimal full-state feedback control with Fox model parameters.

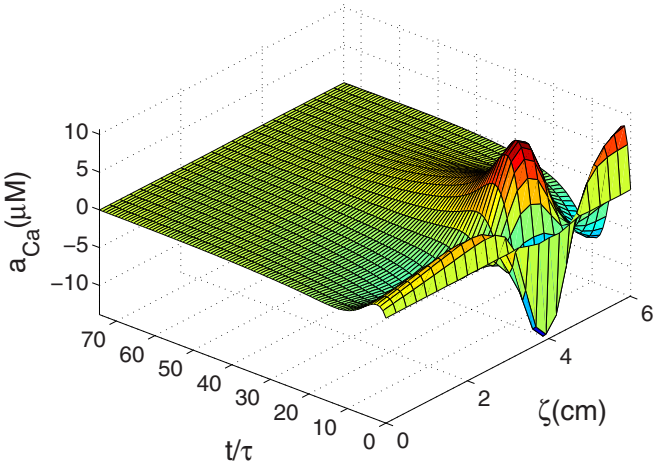

FIG. 7. (Color online) Stabilization of the amplitude of calcium alternans PDE under optimal full-state feedback control with Fox model parameters.

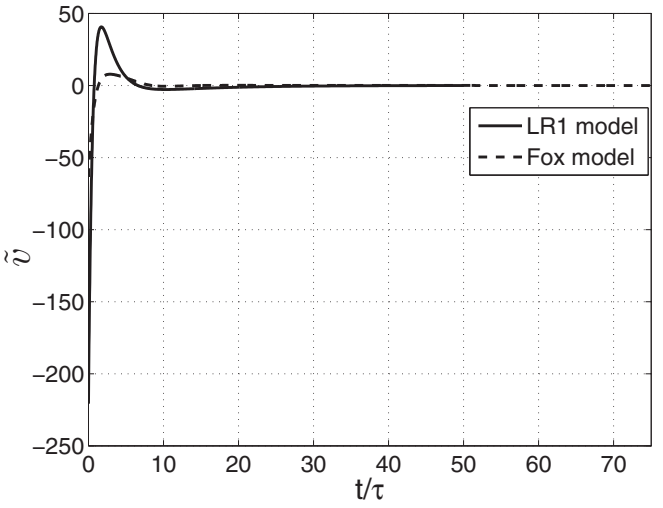

FIG. 9. Trajectories of input derivative $\tilde{v}(t)$ for the LR1 and Fox ionic models under optimal full-state feedback control.

respectively, under this optimal control law. Again, these figures demonstrate that stabilization of all 28 modes of $a(\zeta,t)$ and $a_{Ca}(\zeta,t)$ can be achieved using the low-dimensional optimal controller. The input trajectories $v(t)$, $\tilde{v}(t)$, and $u_{Ca}(t)$ are shown in Figs. 8–10.

It is important to note that although the exponential stabilization of the infinite-dimensional state variables is achieved in both cases, this method does not account for the influence of the feedback control law on the higher (fast) modes. In reality, the higher modes of $\mathcal{A}^e$ may be amplified by the control law. This is known as the spillover effect [22]. In the simulations, this phenomenon is reflected as the high excursion of the state variables away from the boundary pacing site, as shown in Figs. 5–7.

From Figs. 8 and 9, it is apparent that the boundary controller for the LR1 model is significantly more aggressive compared to that for the Fox model. This is because for the LR1 model, the stabilization of $a(\zeta,t)$ must be achieved solely through boundary control. On the other hand, for the Fox model, stabilization is achieved using both boundary and spatial actuation, and as a result aggressive controller actions are not required. This is advantageous for the implementation of the control scheme, since an overly aggressive boundary controller may result in conduction block, which is highly undesirable.

The results obtained from the LR1 model imply that in the case of full-state feedback realization (i.e., full knowledge of the APD state evolution), boundary pacing alone can potentially stabilize alternans along the entire length of the cable. However, in reality this cannot be achieved, because it is impossible to measure the electrical activity at each cardiac cell within the domain.

B. Limitations

An important limitation for the boundary actuator is the fact that the pacing protocol should not postpone the heart's natural

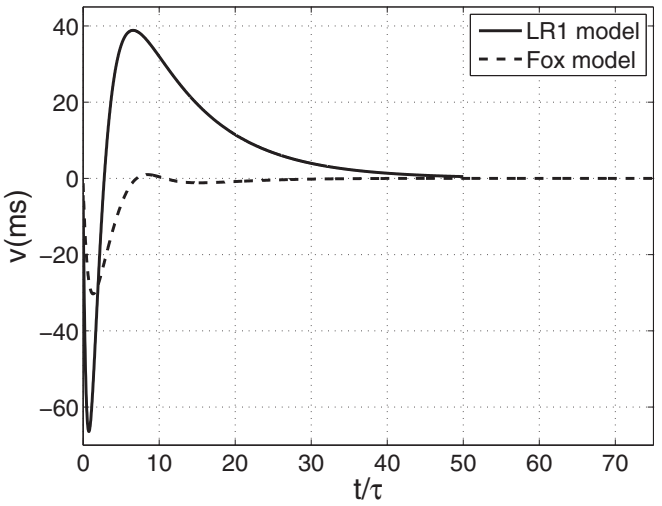

FIG. 8. Trajectories of boundary input $v(t)$ for the LR1 and Fox ionic models under optimal full-state feedback control.

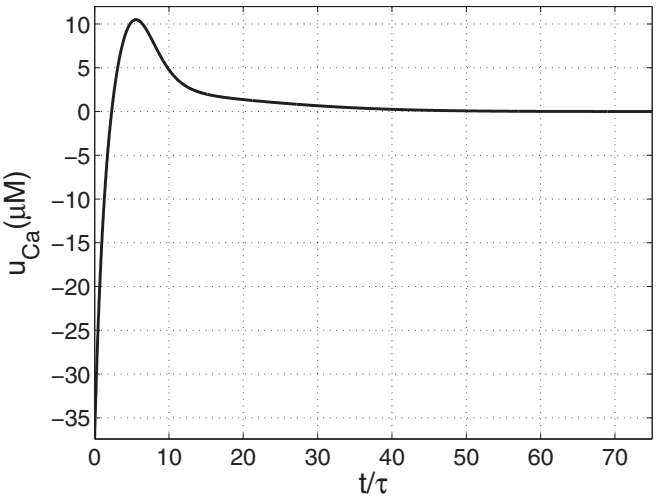

FIG. 10. Trajectory of $u_{Ca}(t)$ for the Fox ionic model under optimal full-state feedback control.

rhythm, which is governed by the sinoatrial node (SAN). In other words, the boundary actuation is constrained to negative perturbations only. This provides the motivation to extend this work further into the framework of model predictive control, such that input constraints can be explicitly accounted for in the controller formulation.

Another natural extension to this method is the development of an optimal output feedback controller, in which measurements of a and a_{Ca} at discrete points along the cable are used to reconstruct their profiles along the entire cable. As shown in [19], if an unstable mode is unobservable, feedback control will not be able to suppress it. Therefore, the number of sensors must be equal to or greater than the number of unstable modes in the system. For a cable length of 6.25 cm, there are two unstable eigenvalues (excluding the zero eigenvalue), so at least two sensors are required for a proper observer design. This is convenient, since the sensors can be placed at either end of the cable. As shown by Figs. 3 and 4, the number of unstable eigenvalues increases with the cable length. Therefore, with longer cables, more sensors will be required.

For the Ca^{2+} based actuator, modulating the intracellular Ca^{2+} concentration affects the tissue's mechanical properties. In general, however, Ca^{2+} is a weak modulator for the heart's mechanical activities compared to a direct mechanical stimulus. Furthermore, measurements of the intracellular Ca^{2+} concentration may not be readily available. Therefore, in the following section, we develop a second control scheme based on the three variable Nash-Panfilov model [31], in which the feedback algorithm applies direct mechanical perturbations to the cable. As shown in [29], the the cardiac muscle's contractile act coincides with the electric wave back. Applying a mechanical stimulus to the cable will affect the wave back, therefore altering the APD [29,30].

IV. ELECTROMECHANICAL MODEL

In this section, we utilize the three variable Nash-Panfilov (NP) model [31] to reconstruct the cardiac cell's electrical and mechanical properties. The NP model adds a third variable to the well known Aliev-Panfilov model (AP) to describe the active tension in the cell. The active tension, which is a function of the electrical voltage, is then linked to the mechanics model. The purpose of this section is to demonstrate alternans annihilation via mechanical perturbations through the feedback mechanism by relying on nonionic descriptions of the cardiac cell dynamics. While ionic models can reconstruct the action potential in detail by accounting for all possible interactions between the ionic species, the AP model reconstructs cardiac cell dynamics by accounting for the major dynamical features of the action potential coupled with the mechanics of cell contraction.

The mechanical analysis is based on the the finite elastic deformation theory. The finite deformation gradient tensor $\mathbf{F}$, coordinates $\mathbf{x}$ and $\mathbf{X}$, the Cauchy-Green deformation tensor $\mathbf{C}$ and the Lagrange-Green strain tensor $\mathbf{E}$ are defined in Appendix B. In the absence of body forces, conservation of linear momentum gives rise to equilibrium conditions that are expressed in terms of the second Piola-Kirchhoff stress components, where an isotropic hyperelastic model typical of the Mooney-Rivlin materials is introduced to describe the mechanical properties of the tissue:

$$\frac{\partial}{\partial X_m}\left(T_{mn}F^i_n\right) = 0, \tag{40}$$

$$\frac{\partial}{\partial X_m}(S_{mn}) = 0, \quad m,n = 1,2,3. \tag{41}$$

Here, S_{mn} is the first Piola-Kirchoff stress tensor while T_{mn} is the second Piola-Kirchoff stress tensor given as

$$T_{mn} = T^{\text{passive}}_{mn} + T^{\text{active}}_{mn}. \tag{42}$$

T^{active}_{mn} has components that are obtained from the electrophysiological model and is responsible for the mechanical deformations. The individual components of T^{passive}_{mn} and T^{active}_{mn} are given by

$$T^{\text{passive}}_{mn} = T^{W}_{mn} - p(C_{mn}), \tag{43}$$

$$T^{W}_{mn} = \frac{1}{2}\left(\frac{\partial W}{\partial E_{mn}} + \frac{\partial W}{\partial E_{nm}}\right), \tag{44}$$

$$T^{\text{passive}}_{mn} = \frac{1}{2}\left(\frac{\partial W}{\partial E_{mn}} + \frac{\partial W}{\partial E_{nm}}\right) - p(C_{mn}), \tag{45}$$

$$T^{\text{active}}_{mn} = T_a C_{mn}, \tag{46}$$

where $E_{nm} = (E_{mn})^T$ are Green's strain components, $C_{mn} = (C^{mn})^{-1}$, p is the pressure, T_a is the active stress, and W is the strain energy function defined as

$$W = c_1(I_1 - 3) + c_2(I_3 - 3),$$
$$I_1 = \text{tr}(\mathbf{C}), \quad I_2 = \tfrac{1}{2}[(\text{tr}(\mathbf{C}))^2 - \text{tr}(\mathbf{C}^2)], \quad I_3 = \det(\mathbf{C}), \tag{47}$$

where c_1 and c_2 are material constants. Here, I_1, I_2, and I_3 are the principal invariants of the Cauchy-Green stress tensor, $\mathbf{C}$, and tr($\mathbf{C}$) is the trace of $\mathbf{C}$, which is the sum of its principal diagonal elements.

Equations governing the electrophysiological variables of the one-dimensional NP model are described as follows:

$$\bar{C}_m \frac{\partial V}{\partial t} = D\frac{\partial}{\partial X_i}\left(\sqrt{C}C^{mn}\frac{\partial V}{\partial X_i}\right) - f(V), \tag{48}$$

$$\frac{\partial r}{\partial t} = \left(\varepsilon + \frac{\mu_1 r}{\mu_2 + V}\right)[-r - kV(V - a - 1)], \tag{49}$$

$$\frac{\partial T_a}{\partial t} = \epsilon(V)(k_{Ta}V - T_a), \tag{50}$$

$$\frac{\partial S_{mn}}{\partial X_m} = 0, \tag{51}$$

where all parameters and variables are dimensionless. $\bar{C}_m = 1$ represent the membrane capacitance, V is the transmembrane potential, $D = 1$ is the diffusivity constant, $C = \det(\mathbf{C})$, $f(V) = kV(V - 1)(V - a) - rV - I_g$, a is the threshold parameter, r is the recovery variable, I_g is the stretch-activated current, and k_{Ta} is a parameter that controls the amplitude of T_a. T_a is assumed to depend directly on the trans-membrane potential, with a delay fixed by $\epsilon(V)$, which is given by 0.1 for $V < a$ and 1.0 for $V > a$. The parameters ε, k, μ_1, and μ_2 have no clear physiological meaning, but are fitted to reproduce the key characteristics of the cardiac tissue [31].

The electrophysiological model described by (48)–(50) coupled with the cardiac mechanics described in Appendix B and (40)–(47) together form the NP model. The term $\mathbf{F} = \partial\mathbf{x}/\partial\mathbf{X}$ introduces nonlinearity in the system and requires the usage of rigorous numerical techniques to ensure computational stability. Hence, a linear approximation for $\mathbf{F}$ is employed and the model is simulated as a coupled system, as similarly presented in [34]. When only one dimension is relevant, $\mathbf{F}$ and $\mathbf{C}$ can be written as

$$\mathbf{F} = \begin{bmatrix} F(X) & 0 & 0 \\ 0 & 1 & 0 \\ 0 & 0 & 1 \end{bmatrix}, \quad \mathbf{C} = \begin{bmatrix} F^2(X) & 0 & 0 \\ 0 & 1 & 0 \\ 0 & 0 & 1 \end{bmatrix}. \tag{52}$$

By computing the derivatives in (44), the one-dimensional (1D) mechanics equations can be reduced to

$$\mathbf{T}^W = 2c_1\mathbf{I}, \tag{53}$$

$$\mathbf{S}^W = \mathbf{T}^W\mathbf{F}' = 2c_1\mathbf{F}, \tag{54}$$

$$\mathbf{S}^{\text{passive}} = \mathbf{S}^W + p\,\det(\mathbf{F})\mathbf{F}^{-1}, \tag{55}$$

where $\mathbf{F}'$ denotes the transpose of $\mathbf{F}$. The last term in (55), which is nonzero in the absence of external forces for incompressible materials [for which $\det(\mathbf{F}) = 1$], maintains the isotropic conditions. By enforcing the condition $\mathbf{S}^{\text{passive}} = 0$ when $F(X) = 1$, we obtain $p = -2c_1 = -\tilde{c}$. Hence, the complete stress which is given by $\mathbf{S} = \mathbf{T}\mathbf{F}' = \mathbf{S}^{\text{passive}} + \mathbf{S}^{\text{active}}$ can be written as

$$\mathbf{S} = \mathbf{S}^W - \tilde{c}\,\mathbf{F}^{-1} + T_a\mathbf{C}^{-1}\mathbf{F}'. \tag{56}$$

From (51), we obtain

$$\frac{\partial}{\partial X}\left[S_{11}^W + p + \frac{T_a(X)}{F(X)}\right] = 0,$$

$$\frac{\partial}{\partial X}\left[\tilde{c}[F(X) - 1] + \frac{T_a(X)}{F(X)}\right] = 0. \tag{57}$$

Neglecting the constant pressure term, (57) becomes

$$\frac{\partial}{\partial X}\left[\tilde{c}F(X) + \frac{T_a(X)}{F(X)}\right] = 0. \tag{58}$$

For small (linear) deformations, we apply the approximation $F(X) = 1 + u(X)$, where $u(X)$ is the instantaneous deformation, and $u \ll 1$. Integrating (58) using this approximation (see [34]), we obtain

$$F(X) = 1 + u(X) = \frac{[A - T_a(X)]}{\tilde{c}}, \tag{59}$$

where A is a constant of integration to be determined. Applying the boundary conditions [$x(0) = 0$ and $x(L) = L$] yields

$$\int_0^L F(X)dX = L \tag{60}$$

and thus

$$A = \tilde{c} + \bar{T}_a, \quad \bar{T}_a = \frac{1}{L}\int_0^L T_a(X)dX, \tag{61}$$

$$F(X) = 1 + \frac{[\bar{T}_a - T_a(X)]}{\tilde{c}}. \tag{62}$$

At any particular position, $\bar{T}_a > T_a$ signifies that the cable is elongated or stretched. The current I_g in $f(V)$ [see Eq. (48)] is active only when the cell stretches locally and it is given as

$$I_g = (g/\tilde{c})(V - 1)(\bar{T}_a - T_a)^2. \tag{63}$$

TABLE II. Parameter values for the electromechanical model.

$k = 8$	$a = 0.05$	$\varepsilon = 0.1$	$\mu_1 = 0.12$
$\mu_2 = 0.3$	$k_{Ta} = 47.9$	$\tilde{c} = 16$	$g = 1.6$

For the purpose of numerical simulations, (48)–(51) are used to constitute the electromechanical model while the mechanical deformation gradient is given by (62). A one-dimensional cable of length $L = 7$ cm is considered. $\mathbf{F}$ is evaluated numerically using the semi-implicit finite difference time integration scheme, namely the first order forward-backward Euler method [35], with $\Delta t = 0.02$ and $\Delta X = 0.1$. All model parameters used in the simulation are given in Table II. The cable is paced at the boundary to its critical pacing length (PL) such that the APD alternates. For the given parameters, the critical period is found to be 66 time units. As outlined in [31], to determine the scaling factor for the dimensionless time unit, the dimensionless APD obtained from the model must be compared to experimental measurements. Scaling factors ranging 5–14 ms have been reported [36–38]. For the dimensionless space variable, one dimensionless unit corresponds to 1 mm [37], which links the NP model to other relevant electrophysiological models. The APD is measured from the instant V crosses a threshold value during the depolarization phase, until the instant it falls below this value during the repolarization phase. The threshold value was chosen to be 0.4 (in dimensionless units). The amplitude of alternans is given by the difference between two consecutive APDs. As shown by Fig. 11, without control and under constant critical PL, the amplitude of alternans grows until it reaches a plateau.

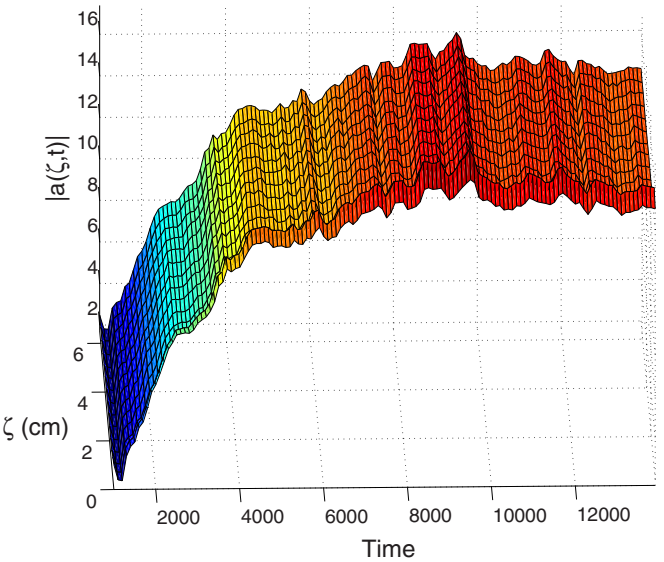

FIG. 11. (Color online) Magnitude of the amplitude of alternans for the Nash-Panfilov (NP) model. The cable is paced at 66 time units, which is the critical pacing length.

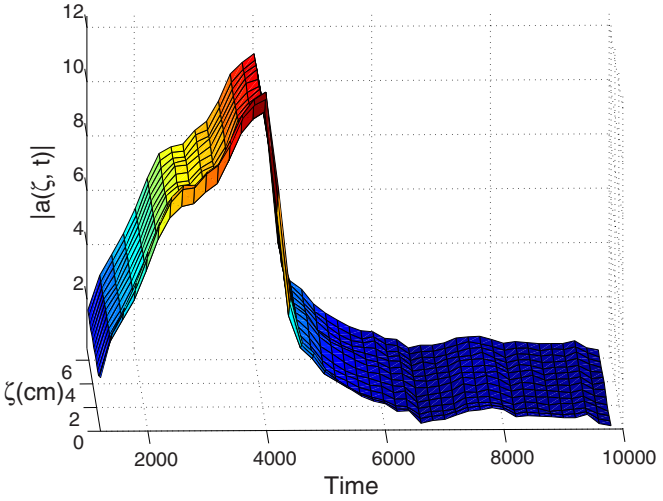

FIG. 12. (Color online) Amplitude of alternans Nash-Panfilov (NP) model. The cable is paced 66 time units, at which the amplitude of alternans grow until control is applied at $t = 4000$.

A spatially distributed, mechanic based control algorithm is implemented on the cable to annihilate alternans. Basic full state feedback algorithm which takes the error $e_n(t)$ [defined in Eq. (65)] generated between two consecutive APDs provides a control signal which is applied over the region 3–4.5 cm. The control signal is active only when $e_n(t) < 0$ meaning that the controller only acts on the long-APD [see Fig. 13(b) after $t = 4000$, when the controller is activated]. Incorporating the spatially distributed controller into (50), the following error based control scheme is obtained:

$$\frac{\partial T_a}{\partial t} = \epsilon(V)(k_{Ta}V - T_a) + \beta e_n(t), \tag{64}$$

$$e_n(t) = (\mathrm{APD}_n - \mathrm{APD}_{n-1}), \tag{65}$$

where β is the controller gain. In the simulation, $\beta = -0.0003$. This control action alters the cable's membrane potential through mechanoelectric feedback, in which changes in T_a alter the stretch-activated current I_g, which then affects (48) through $f(V)$. As shown by Fig. 12, this control algorithm can successfully annihilate alternans along the cable.

Figures 13(a) and 13(b) show the evolution of the membrane potential and the deformation variable, respectively, before and up to the application of control. Figures 14(a) and 14(b) show the evolution of the same variables after control is applied. The controller action applied over the region [3,4.5] cm on the long (L) APD can be seen in Fig. 13(b). From Figs. 12 and 14, we see that after the the spatially distributed mechanical stress-strain based controller is activated at $t = 4000$, both electrical and mechanical alternans are annihilated. Although the controller is only applied over a localized region of the cable [see Fig. 13(b)], it affects the entire length of the cable, successfully annihilating alternans along the cable. Thus, using a model based on the mechanical and electrophysiological properties of the cardiac tissue, it is clearly shown that mechanical perturbations can be used to manipulate the electrical APD in order to suppress alternans.

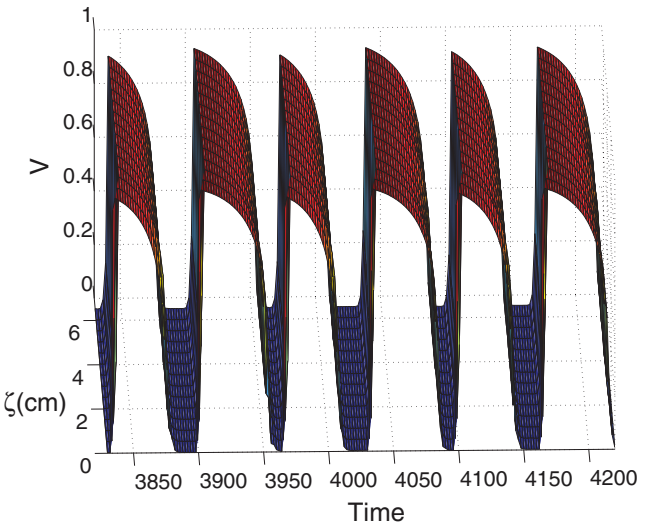

(a)

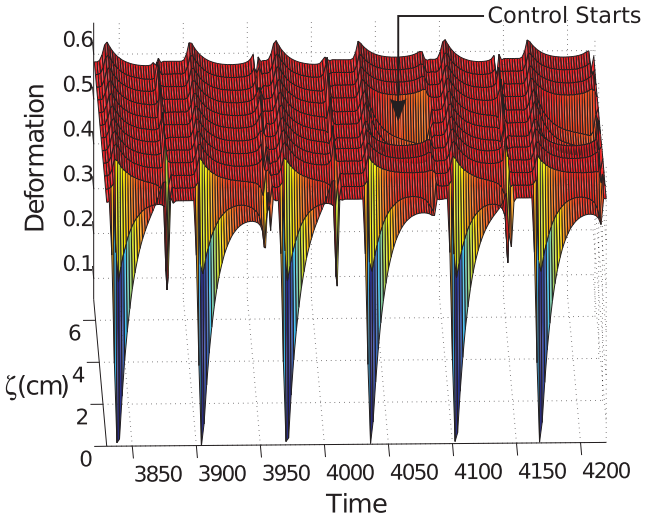

(b)

FIG. 13. (Color online) Time evolution of membrane potential and deformation variable showing alternans. (a) Membrane potential. (b) Deformation variable x_i. Control is applied at $t = 4000$ over the region [3,4.5] cm, as denoted by the arrow in (b).

V. CONCLUSION

In this paper, an optimal full-state feedback control scheme is developed for the coupled system of PDEs describing the dynamics of the small amplitude of cardiac alternans and the peak intracellular Ca^{2+} concentration alternations along a 1D cable of cardiac cells. This control scheme combines a pacer applied at the boundary and a spatially distributed, Ca^{2+} based controller. The optimal control law is obtained by solving the standard LQR problem. Simulations were performed using PDE parameters obtained from the LR1 ionic model and the Fox ionic model. In both cases, we demonstrated the successful annihilation of cardiac alternans along a 6.25-cm cable of cardiac cells. In practice, direct measurements of the intracellular Ca^{2+} concentration and its alternations are difficult. Hence, a mechanical stretch based distributed control

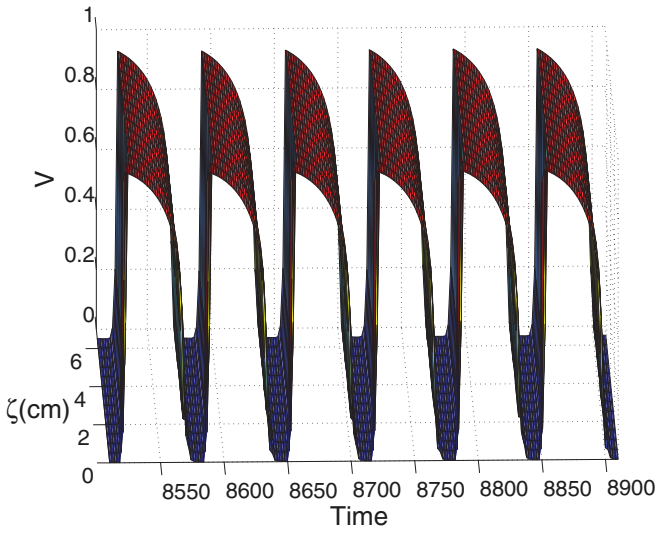

(a)

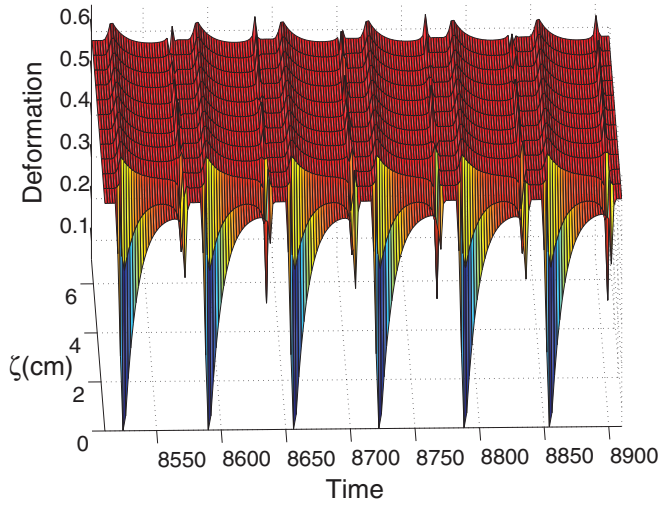

(b)

FIG. 14. (Color online) Time evolution of membrane potential and deformation variable x_i after control is applied. (a) Membrane potential. (b) Deformation variable x_i. As shown by both (a) and (b), the control action successfully annihilates alternans in both variables.

was considered. We then demonstrated that this stretch based control protocol can suppress alternans in a 7-cm-long cable of cardiac cells simulated using the Nash-Panfilov model.

The annihilation of cardiac alternans using feedback control has been studied extensively. However, it has been found that control strategies that are solely voltage based are only effective close to the control site. Away from the pacing site, alternans will continue growing, eventually leading to conduction block. In this work, we have demonstrated that by the inclusion of a voltage-independent actuator (i.e., calcium based or mechanical based), we can overcome this limitation in controllability, and achieve alternans annihilation along the entire 6–7-cm cable.

In developing these control strategies, constraints that may be naturally present in the cardiac system were not accounted for. This issue will be addressed in future works, where the input and state constraints are to be included explicitly in the controller formulation. Furthermore, in order to further verify the results presented in this paper, extensive research efforts are being concentrated on realizing the control strategies suggested here onto ionic model(s), as a pacing and Ca^{2+} drug releasing protocol, or a stretching protocol.

ACKNOWLEDGMENTS

This research was supported by the Heart and Stroke Foundation of Canada Grant-in-Aid (GIA). The authors also wish to acknowledge the financial support of the National Science and Engineering Research Council of Canada (NSERC).

APPENDIX A: EIGENFUNCTIONS OF THE PDE SPATIAL OPERATORS

In (18), the spatial derivative operators $\mathcal{A}_1$ and $\mathcal{A}_2$ are Sturm-Liouville operators which can be written in the following form:

$$\mathcal{A}\phi(\cdot) = \frac{1}{\rho(\cdot)}\frac{d}{d\zeta}\left[p(\cdot)\frac{d\phi}{d\zeta}(\cdot)\right] + q(\cdot)\phi(\cdot). \tag{A1}$$

Comparing the coefficients of (A1) with (9) and (16), we obtain $\rho(\zeta) := \exp^{-(\omega/D_a)\zeta}$, $p(\zeta) := D_a\rho(\zeta)$, $q(\zeta) := \sigma$ for $\mathcal{A}_1$, and $q(\zeta) = 0$ for $\mathcal{A}_2$. The eigenvalues for $\mathcal{A}_1$ and $\mathcal{A}_2$ are given by (19) and (20), respectively. For $\mathcal{A}_1$, the eigenfunctions and adjoint eigenfunctions for $i \geqslant 1$ are given by

$$\phi_i(\zeta) = B_i \exp^{(\omega/2D_a)\zeta}\left[\cos(\sqrt{\alpha_i}\zeta) + \frac{1}{\sqrt{\alpha_i}}\left(1 - \frac{\omega}{2D_a}\right)\sin(\sqrt{\alpha_i}\zeta)\right], \tag{A2}$$

$$\phi_i^*(\zeta) = \exp^{-\omega/D_a}\phi_i(\zeta). \tag{A3}$$

The coefficients B_i's are obtained by imposing the orthogonality condition $\langle\phi_i(\zeta),\phi_j^*(\zeta)\rangle = \delta_{ij}$, and are evaluated as

$$B_i = \left\{\int_0^L \left[\cos(\sqrt{\alpha_i}\zeta) + \frac{1}{\sqrt{\alpha_i}}\left(1 - \frac{\omega}{2D_a}\right)\sin(\sqrt{\alpha_i}\zeta)\right]^2 d\zeta\right\}^{-1/2}. \tag{A4}$$

For $\mathcal{A}_2$, the eigenfunctions and adjoint eigenfunctions are equal to those of $\mathcal{A}_1$. This is because the PDE parameters in (4) and (5) are equal except for the growth term σ, and the eigenfunctions are independent of this term. Thus,

$$\psi_i(\zeta) = \phi_i(\zeta), \quad \text{and} \quad \psi_i^*(\zeta) = \phi_i^*(\zeta). \tag{A5}$$

APPENDIX B: FINITE ELASTIC DEFORMATION THEORY—DEFINITIONS

In the electromechanical model, the mechanical analysis is based on the the finite elastic deformation theory. The finite deformation gradient tensor $\mathbf{F}$ that transforms the undeformed cell geometry to a deformed state is given as

$$F_m^i = \frac{\partial x_i}{\partial X_m}, \quad \mathbf{F} = \frac{\partial \mathbf{x}}{\partial \mathbf{X}}, \quad i,m = 1,2,3, \tag{B1}$$

where **x** is a vector denoting the positions of the particles in the deformed coordinates (x_i's) while **X** consists of X_m's, which denote the reference (undeformed) material coordinates. Therefore, **F** represents a map that transforms a material line segment from an undeformed geometry $d\mathbf{X}$ to a deformed geometry $d\mathbf{x}$. The Cauchy-Green deformation tensor **C** and Lagrange-Green strain tensor **E** are respectively defined as

$$\mathbf{C} = \mathbf{F}^T\mathbf{F}, \quad C^{mn} = \left\{\frac{\partial x_k}{\partial X_m}, \frac{\partial x_k}{\partial X_n}\right\}, \tag{B2}$$

$$\mathbf{E} = \frac{1}{2}(\mathbf{C} - \mathbf{I}), \tag{B3}$$

where **I** is the identity matrix.

[1] G. E. Billman, Am. J. Physiol-Heart C **297**, H1171 (2009).
[2] A. Burke and R. Virmani, in *Encyclopedia of Forensic and Legal Medicine*, edited by J. Payne-James (Elsevier, Oxford, 2005), pp. 211–223.
[3] J. M. Pastore, S. D. Girouard, K. R. Laurita, F. G. Akar, and D. S. Rosenbaum, Circulation **99**, 1385 (1999).
[4] L. Makarov and V. Komoliatova, ANN Noninvas Electro. **15**, 138 (2010).
[5] S. M. Narayan, J. Am. Coll. Cardiol. **49**, 347 (2007).
[6] J.-M. Cao, Z. Qu, Y.-H. Kim, T.-J. Wu, A. Garfinkel, J. N. Weiss, H. S. Karagueuzian, and P.-S. Chen, Circ. Res. **84**, 1318 (1999).
[7] D. S. Rosenbaum, L. E. Jackson, J. M. Smith, H. Garan, J. N. Ruskin, and R. J. Cohen, New Engl. J. Med. **330**, 235 (1994).
[8] Y. Shiferaw, D. Sato, and A. Karma, Phys. Rev. E **71**, 021903 (2005).
[9] Y. Shiferaw and A. Karma, Proc. Natl. Acad. Sci. USA **103**, 5670 (2006).
[10] D. Sato, Y. Shiferaw, A. Garfinkel, J. N. Weiss, Z. Qu, and A. Karma, Circ. Res. **99**, 520 (2006).
[11] D. J. Christini, M. L. Riccio, C. A. Culianu, J. J. Fox, A. Karma, and R. F. Gilmour, Jr., Phys. Rev. Lett. **96**, 104101 (2006).
[12] J. J. Fox, M. L. Riccio, F. Hua, E. Bodenschatz, and R. F. Gilmour, Jr., Circ. Res. **90**, 289 (2002).
[13] S. Sridhar, D.-M. Le, Y.-C. Mi, S. Sinha, P.-Y. Lai, and C. K. Chan, Phys. Rev. E **87**, 042712 (2013).
[14] B. Echebarria and A. Karma, Chaos **12**, 923 (2002).
[15] T. Krogh-Madsen, A. Karma, M. L. Riccio, P. N. Jordan, D. J. Christini, and R. F. Gilmour, Jr., Phys. Rev. E **81**, 011915 (2010).
[16] S. Dubljevic, S. F. Lin, and P. D. Christofides, Comput. Chem. Eng. **32**, 2086 (2008).
[17] S. F. Lin and S. Dubljevic, in *Proceedings of the 2007 American Control Conference* (IEEE, New York, 2007), pp. 600–606.
[18] A. Garzon, R. O. Grigoriev, and F. H. Fenton, Phys. Rev. E **80**, 021932 (2009).
[19] A. Garzon, R. O. Grigoriev, and F. H. Fenton, Phys. Rev. E **84**, 041927 (2011).
[20] S. H. Weinberg and L. Tung, PloS ONE **7**, e40477 (2012).
[21] H. Dvir and S. Zlochiver, Biophys. J. **105**, 533 (2013).
[22] S. Dubljevic and P. D. Christofides, Chem. Eng. Sci. **63**, 5425 (2008).
[23] B. Echebarria and A. Karma, Phys. Rev. Lett. **88**, 208101 (2002).
[24] R. F. Curtain and H. Zwart, *An Introduction to Infinite-Dimensional Linear Systems Theory* (Springer-Verlag, New York, 1995).
[25] W. H. Ray, *Advanced Process Control* (McGraw-Hill, New York, 1981).
[26] P. Hunter, A. McCulloch, and H. ter Keurs, Prog. Biophys. Mol. Biol. **69**, 289 (1998).
[27] P. Kohl, P. Hunter, and D. Noble, Prog. Biophys. Mol. Biol. **71**, 91 (1999).
[28] O. E. Solovyova, N. A. Vikulova, P. V. Konovalov, P. Kohl, and V. S. Markhasin, Russ. J. Numer. Anal. Math. Modell. **19**, 331 (2004).
[29] D. M. Bers, Nature (London) **415**, 198 (2002).
[30] S. C. Calaghan, A. Belus, and E. White, Prog. Biophys. Mol. Biol. **82**, 81 (2003).
[31] M. P. Nash and A. V. Panfilov, Prog. Biophys. Mol. Biol. **85**, 501 (2004).
[32] C. Luo and Y. Rudy, Circ. Res. **68**, 1501 (1991).
[33] J. J. Fox, J. L. McHarg, and R. F. Gilmour, Jr., Am. J. Physiol.-Heart Circ. Physiol. **282**, H516 (2002).
[34] E. Alvarez-Lacalle and B. Echebarria, Phys. Rev. E **79**, 031921 (2009).
[35] M. Ethier and Y. Bourgault, SIAM J. Numer. Anal. **46**, 2443 (2008).
[36] A. V. Panfilov and J. P. Keener, Chaos Soliton Frac. **5**, 681 (1995).
[37] R. R. Aliev and A. V. Panfilov, Chaos, Solitons Frac. **7**, 293 (1996).
[38] A. V. Panfilov, Chaos **8**, 57 (1998).